GelPoLight: A Novel Visual Tactile Sensor Based on Photometric Stereo with Point Lighting

Chuang Lu, Ziting Liang *Graduate Student Member, IEEE*, Danail Stoyanov *Fellow, IEEE*, Agostino Stilli, *Member, IEEE*

***Abstract*— Visual tactile sensors based on photometric stereo (VTS-PS) have attracted much attention due to their sensitivity to subtle contact forces and their capability of providing real-time, high-resolution depth maps of contact geometry at a low cost. Conventional VTS-PS, such as Gelsight, typically assume directional and uniform illumination to simplify the algorithm of photometric stereo. However, this assumption poses stringent requirement on the hardware side and limits the sensors in shape, size and flexibility for various applications. Additionally, the configuration of directional lighting exacerbates the issue of cast shadowing. In this paper, We analyse the benefits of point lighting over conventional directional lighting for VTS-PS, and propose GelPoLight: a novel VTS-PS with point lighting, which can help handle or alleviate the aforementioned problems. GelPoLight does not assume ideal diffuse reflectance for the reflective membrane and considers the varying influencing factors of light intensity, light directions, and reflectance factors in the estimation of surface normal vectors. Accordingly, we developed a new calibration method for this approach. We also corrected image distortions caused by light refraction, which is a prevalent issue in visual tactile sensors (VTS). The final results demonstrate that GelPoLight can effectively generate the contact depth map, with errors of approximately 5% in planar direction and 8% in depth direction.**

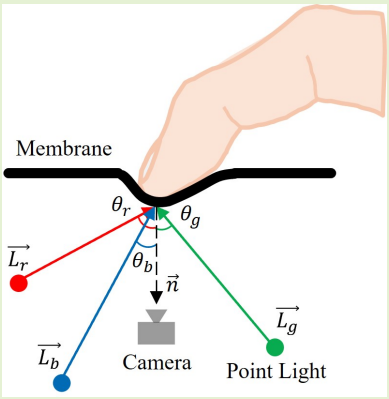

***Index Terms*— visual tactile sensor, photometric stereo, Gelsight, directional lighting, point lighting, cast shadowing, surface normal vector, light refraction, depth maps, diffuse reflectance**

I. Introduction

TOUCH, a critical form of perception for both human beings and robots to interact with the external world, encompasses pressure, shape, texture and temperature. Over the past few decades, numerous studies have focused on developing compact tactile sensors aimed at achieving and surpassing the performance of human fingers. Conventional approaches, such as those based on piezoelectric [1], piezoresistive [2], capacitive [3], triboelectric [4], and optical [5] principles, have demonstrated good performance in detecting contact forces. Plasmonic optical fiber sensors have seen significant advancements in molecular detection, such as the newly developed WaveFlex Biosensor [6]. Advancements in micro-electromechanical systems (MEMS) technology have enabled the integration of multiple sensing elements, resulting in miniaturisation, high precision, and improved reliability [7]. However, providing sufficient high resolution in a limited area remains a significant challenge, impacting the sensing of precise contact geometry of the objects being touched.

Visual tactile sensors (VTS) utilise images as media to visually represent contact deformations, with each pixel functioning as an individual sensing element. Thanks to the advancements of camera technology, these class of sensors can achieve high resolution at a low cost. GelSight, one of the most well-known VTS, is capable of generating real-time depth maps of contact geometry with micron-level resolution based on the principle of photometric stereo [8]. However, GelSight and derivative designs assume directional and uniform illumination to satisfy photometric stereo conditions. This stringent lighting requirement poses challenges on the optical design and fabrication, and limits the sensors in shape, size, and flexibility for various applications. Additionally, these sensors suffer from cast shadowing issues and exhibit weaknesses in measuring large deformations.

In this paper, we introduce GelPoLight, a novel visual tactile sensor based on photometric stereo (VTS-PS) with point lighting. The paper first analyses the benefits of point lighting over previous directional lighting, followed by the structural design and fabrication methods, and then propose a new calibration method for this approach. The contributions of this paper are:

1) Proposing point lighting method for VTS-PS, and

This work was supported in part by the Wellcome/EPSRC Centre for Interventional and Surgical Sciences (WEISS) under Grant 203145/A/16/Z and in part by the Royal Academy of Engineering Chair in Emerging Technologies Scheme under Grant CiET1819/2/36. For the purpose of open access, the authors have applied a CC BY public copyright licence to any author accepted manuscript version arising from this submission (Corresponding author: Agostino Stilli).

Chuang Lu, Ziting Liang, Danail Stoyanov, and Agostino Stilli are with the UCL Hawkes Institute, University College London, WC1E 6BT London, UK (e-mail: chuang.lu.22@ucl.ac.uk; ziting.liang.21@ucl.ac.uk; danail.stoyanov@ucl.ac.uk; a.stilli@ucl.ac.uk).

analysing the advantages of point lighting in place of directional lighting.
2) Developing the structural design and fabricating methods for the proposed sensor.
3) Introducing a new experiment-based calibration method for this approach.
4) Addressing an image correction method to rectify distorted images caused by refracted light for VTS.

II. Related Works

Photometric stereo assumes that while holding a fixed position of camera, for each image point illuminated by light in three directions

$$\vec{L} = \begin{bmatrix} L_{1_x} & L_{1_y} & L_{1_z} \\ L_{2_x} & L_{2_y} & L_{2_z} \\ L_{3_x} & L_{3_y} & L_{3_z} \end{bmatrix}$$

the surface orientations $\vec{n} = \begin{bmatrix} n_x & n_y & n_z \end{bmatrix}$ at this point can be determined when the surface reflectance factors ρ and the image pixel values $I = \begin{bmatrix} I_1 & I_2 & I_3 \end{bmatrix}$ are identified, provided the light vectors do not lie in a plane [9], shown as below:

$$I = \rho \cdot \vec{n} \cdot \vec{L} \tag{1}$$

To apply the above principle for VTS-PS and simplify the algorithm, GelSight assumes that the light vectors $\vec{L}$ and the reflectance factor ρ remain constant [8], thus the surface normal vectors $\vec{n}$ can be determined solely by the triplet pixel values I, shown as below:

$$\vec{n} = \mathcal{F}(I) \tag{2}$$

Significant efforts have been made in VTS-PS to improve the reflectance properties of the membranes and the illumination systems to satisfy the above assumption. Li et al. in [10] designed a compact sensor with optical guides for directional lighting and a semi-specular membrane to amplify the reflection. Dong et al. in [11] developed the sensor by applying a matte membrane for better reflectance properties, LED arrays with small radiance angles for directional lighting, and a semitransparent hexagonal plastic tray for uniform illumination. Gray filters and diffusers were used in GelSight Wedge to reduce internal reflections and provide uniform global illumination [12]. The lighting system was further improved in GelSlim 3.0 by shaping the lens and the elastomer to further collimate the light and optimise the distribution of light intensities [13].

To extend the functionality, specially designed markers were incorporated onto the membrane of VTS-PS to track the deformation, which can be used to infer shear force and slip [14]. An elastic suspension structure was integrated into VTS-PS to enhance the three-axis force sensing [15]. In addition to robotic grasping tasks, various applications were explored, including surface texture recognition, hardness estimation, and lump detection [16]–[18]. VTS-PS were also developed into different size and shape for different purposes. DIGIT miniaturised its form-factor to be mountable on multi-fingered hands [19]. GelSlim [20] was designed to have a slim body by employing a mirror for the view of the camera. GelSight Svelte [21] was developed in the shape of human finger with large sensing coverage by using curved mirrors and flexible backbone.

Tactile sensors with curved surfaces offer enhanced conformity to complex shapes, increasing their applicability in various fields. A rounded fingertip sensor which relies on light piping method for directional illumination was proposed [22]. The semi-specular surface reduces diffuse light loss, and total internal reflection (TIR) maintains light consistency to some extent. However, the above losses still have a significant impact on the sensor performance. GelSight360 [23] with cross-structured LEDs was then developed. However, the cross-illumination strategy employed results in a partial occlusion of the sensing area. Meanwhile, maintaining consistent light directionality and uniformity across the surface is difficult, particularly around the intersections of the LED crossing structures. Multiple research teams have developed other sensors with curved surfaces, such as Digger Finger [24], OmniTact [25], and GelTip [26]. While these teams have further improved on the original design, they have not been able to provide depth maps with their sensors.

Cast shadowing is a common issue in VTS-PS. Johnson et al. in [27] have mitigated the impact of shadows by building up an illumination model, adjusting pixel weights, and smoothing surface normal estimates . Additionally, a method for image shadow detection and compensation was proposed in [28].

To minimise space occupation in compact scenarios, some sensing devices based on VTS-PS, such as [29], [30], employ single LEDs for illumination. However,they usually apply CNNs for object recognition or force estimation instead of providing depth maps, as single LEDs are unable to deliver uniform and directional lighting to satisfy the lighting requirement in conventional VTS-PS.

III. Comparison of Point and Directional Lighting for VTS-PS

Illumination systems are essential for VTS-PS. The assumption of uniform and directional lighting does simplify the working principle. However, directional lighting is inherently limiting, aside from the stringent requirements it imposes on the hardware side.

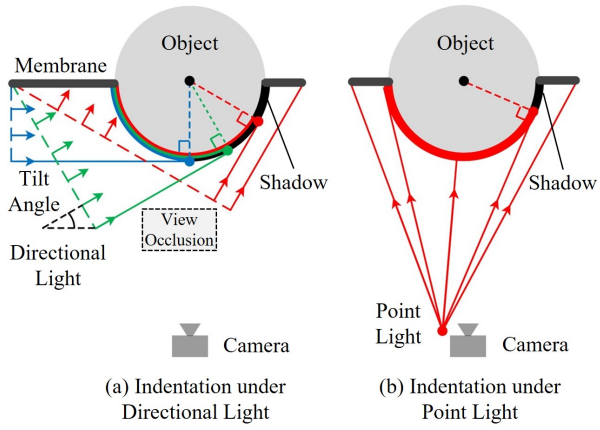

Fig. 1. Lighting Shadow under Directional Light and Point Light

As shown in Fig. 1(a), directional light sources typically consist of arrays of LEDs placed onto the sides of the sensor. However, side lighting with small tilt angles can result in inadequate illumination for the membrane. Using multiple high-brightness LED arrays with bigger tilt angles can mitigate this issue, but it will increase the bulk of the light source. With the increase of the tilt angle, the light-emitting area required to fully illuminate the membrane expands, which either increases the diameter of the sensor or obstructs the field of view of the camera. Besides, the light radiance across the membrane cannot be kept at a constant value due to the varying light propagation distance between each LED and the membrane.

Directional lighting system in VTS-PS exacerbates the issue of cast shadowing. The indentation of the membrane will partially obstruct the light path due to the rectilinear propagation of light, causing some areas to not be illuminated. Directional light with small tilt angles can produce large shadows, especially for sharp deformations. This issue is further intensified for the three light sources required in the sensors, as the area that can be simultaneously illuminated without shadows becomes smaller.

The above issues can be significantly mitigated by replacing the directional lighting with point lighting, as shown in Fig. 1(b). A point light source emits light in all directions, allowing a single LED to fully illuminate the membrane, also when the surface of the targeted membrane is curved. Its compact size allows flexible positioning beneath the elastomer for direct illumination, ensuring sufficient light intensity while minimizing spatial constraints. In addition, point light usually has a large tilt angle, thereby producing relatively small shadows.

Due to these advantages, point lighting has significant benefits over directional lighting for VTS-PS. However, point lighting introduces spatial variability in light direction and radiance, rendering the working principle in GelSight ineffective. Consequently, the development of a new calibration method for VTS-PS with point lighting is anticipated.

IV. Sensor Structure and Fabrication

As illustrated in Fig. 2, the proposed sensor consists of three main parts: (1) the top part features a clear silicone elastomer covered by an opaque reflective membrane, housed in a 3D-printed elastomer casing; (2) the middle part includes a 3D-printed LED holder with three colored point LEDs and a transparent acrylic window fixed onto it; (3) the bottom part contains a camera module within its 3D-printed housing. The three parts are connected together with screws. The external sensor casing is cylindrical, with a diameter of 30 mm and a length of 68 mm. The effective working area is a circular region with a diameter of 26 mm. When an object is pressed onto the sensor, the elastomer deforms and the membrane conforms to the shape of the object. And the membrane diffusely reflects the incident light, allowing the camera to capture the geometry of the object.

A. Elastomer

The elastomer is a soft, elastic, clear silicone slab with flat and transparent top and bottom surfaces, ensuring that the camera view is unobstructed, allowing light to travel in straight lines. The stiffness of the elastomer should be tailored to specific applications: a softer elastomer increases the sensitivity of the sensor to small contact forces, while a harder elastomer can withstand greater forces.

Clear and colourless platinum-cure silicone rubber Solaris™ and silicone tactile mutator Slacker™ (both from Smooth-On, Inc., Macungie, PA, USA) were used to fabricate the elastomer. Slacker™ reduces the stiffness of the elastomer but increases its viscoelasticity, resulting in slow recovery after deformation. The mix ratio by volume for Solaris™ Part A, Solaris™ Part B, and Slacker™ is 1:1:3. This ratio has been tested to ensure the sensitivity of the sensor while maintaining an appropriate recovery time.

After thoroughly mixing, the silicone mixture was placed in a vacuum chamber to degas until bubbles stopped surfacing. The silicone mixture was then poured into a hollow 3D-printed mould for the desired shape. Meanwhile, two clean acrylic sheets sandwiched the mould on the top and bottom with pressure to ensure both surfaces were smooth and transparent. The silicone mixture was cured for 12 hours at room temperature.

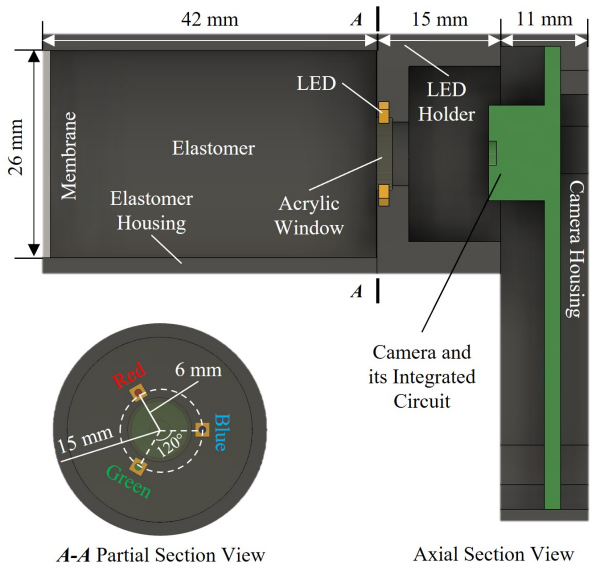

Fig. 2. Axial and Partial Section View of Proposed GelPoLight

B. Membrane

The performance of the sensor highly depends on the membrane: (1) the membrane is supposed to be thin to adequately measure small contact deformations; (2) the reflectance properties of the membrane should be well balanced considering that a gradual pixel-gradient response will miss small deformations, while a steep response can exceed the detection range of the camera; (3) the membrane ought to be opaque to prevent external light interference; (4) the membrane needs to be robust enough to handle normal stretching and be firmly attached to the elastomer.

A fabrication method for this sensor is presented in this paper. First, a small amount of aluminum powder (NANOGRAFI Co. Inc., Camsdorfer Ufer, Germany) is applied to the top surface of the elastomer. The aluminum powder has a spherical

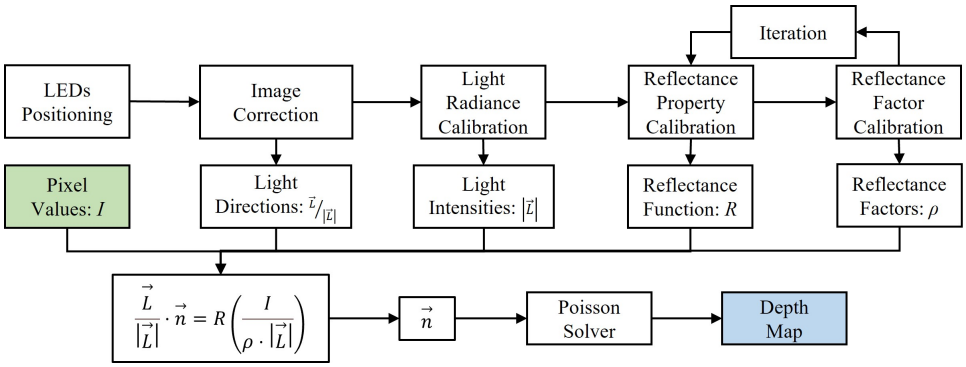

Fig. 3. Calibration Process Flow Chat

morphology with a particle size range of 1-2 microns. The powder is gently rubbed onto the elastomer using a makeup sponge. After that, the excess aluminum powder is blown away using a controlled air stream ejected through a nozzle by an air compressor. As the aluminum powder naturally adheres to the silicone elastomer, a very thin and uniform layer can be formed. Next, Print-On® gray silicone ink and its catalyst (Raw Material Suppliers, Pomona, CA, USA) are mixed and diluted with NOVOCS™ Matte (Smooth-On, Inc., Macungie, PA, USA) in a volume ratio of 10:1:40. The thinned mixture is then sprayed onto the aluminum layer using airbrush to form an opaque protective coating. Finally, The elastomer covered by the membrane is dried in an oven at 50°C for 8 hours to ensure the membrane adhered firmly to the elastomer.

C. LEDs

The emitting areas of the LEDs are expected to be relatively small compared to the area of the membrane. Therefore, the LEDs can be considered as point light sources, which helps determine the direction of light. The radiation angles of the LEDs are anticipated to be wide to ensure the membrane has no overly bright or dark areas. Additionally, the color of the LEDs should be close to pure blue, green, and red to ensure each colour only affects its respective colour channel in the images.

Standard 0201 SMD LEDs of blue, green, and red (LITE-ON Technology Corp., New Taipei City, Taiwan Region) were chose for GelPolight. The LEDs have an outer dimension of 0.3 x 0.6 x 0.2 mm and a wide radiation angle of 120°. The light-emitting area is smaller as only the central part of the LEDs emits light. The LEDs were soldered onto small copper-clad boards and then fixed onto the 3D-printed LED holder, configured at 120° with each. The small air gaps between the LEDs and the elastomer were filled with the same silicone rubber material used for the elastomer to prevent light reflection and refraction at the interface.

D. Camera

The camera used in GelPoLight is a low-cost, fixed focal length, manual focus camera, Logitech C310 HD Webcam (Logitech International S.A., Lausanne, Switzerland). The camera has a view angle of 60°, a frame rate of 30 fps, and a maximum video resolution of 1.2 megapixels. The lens was manually focused near the membrane and then secured to prevent shift in the focus position. The camera functions of auto light correction and auto white balance were disabled. The camera settings, including exposure, brightness, contrast, and white balance, were manually adjusted using Logitech Webcamera Software 2.80 to ensure the images were within an appropriate range of pixel values, preventing overexposure or underexposure. These settings were maintained consistently.

E. Acrylic Window and Elastomer Housing Painting

The acrylic window ensures a clear view for the camera and supports the upper elastomer. A 2-mm-thick acrylic sheet was laser-cut to the desired shape to be fixed onto the slot of the LED holder. The upper surface of the acrylic window can naturally adhere to the bottom surface of the silicone elastomer. Both surfaces need to be kept clean to prevent air bubbles, as these can affect the image quality.

While the light sources illuminate the membrane, they also illuminate the inner wall of the elastomer housing. The reflected light from the inner wall might impact the estimation of the lighting conditions of the sensor. The inner wall of the elastomer housing was painted with Musou Black acrylic paint (KOYO Orient Co.,Ltd, Saitama Prefecture, Japan) to absorb light. The paint was diluted with water at a ratio by volume of 4:1. After thorough mixing, it was used to evenly paint the inner wall using a dust-free swab several times until no visible reflected light was observed.

V. Sensor Calibration

A calibration method based on photometric stereo and with the assumption of point lighting was proposed for GelPoLight. As fabricating a membrane that behaves as an ideal diffuse reflector under laboratory conditions is difficult, the reflectance function of GelPoLight is supposed to be experimentally calibrated rather than assuming Lambertian reflectance. Since light directions, light radiance, and surface reflectance factors are all influencing factors, it is not feasible to directly obtain mappings between pixel values and surface gradients.

As described in Fig. 3, the applicable method mainly involves the following steps:

1) Calibrating the parameters including light direction vectors, the distribution of light intensities, and the distribution of reflectance factors.
2) Processing the pixel values and eliminating the influence of the variation in light radiance and reflectance factors.

3) Exploring the mapping between the processed pixel values and the angles between light direction vectors and surface normal vectors.
4) Establishing the connection between pixel values and surface normal vectors, and estimating the depth map.

A. LEDs Positioning

The positions of the light-emitting points help determine the direction vectors of the incident light at each image point. An calibration method using specular reflection was implemented to estimate the positions of these points. This method was conducted before the acrylic window and the elastomer were installed onto the sensor.

The following parameters were obtained prior to the implementation of this method: (1) the focal length f and the optical centre of the camera were determined using the conventional checkerboard calibration method, and the lens distortions were also corrected; (2) the distance between the optical centre and the top surface of the sensor $Z_1 + Z_2$ was estimated using the Perspective-n-Point (PnP) pose computation method. This estimation was achieved by placing a checkerboard on the top surface of the sensor and using its corner points for the pose computation; (3) the distance from the point light source to the top surface of the sensor Z_1 was derived from the dimensions of the 3D-printed elastomer housing.

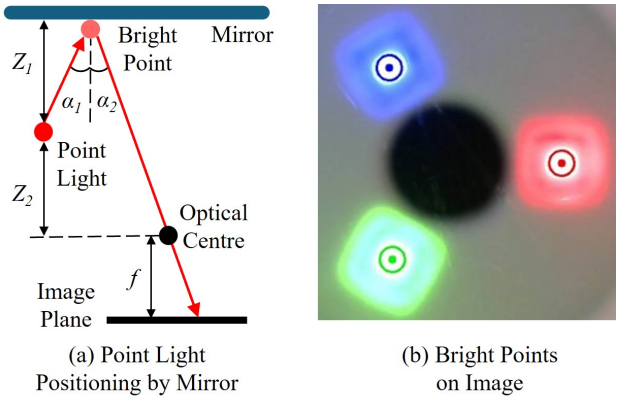

(a) Point Light Positioning by Mirror

(b) Bright Points on Image

Fig. 4. Positioning of Light Emitting Points

As shown in Fig. 4(a), a mirror was placed onto the top surface of the sensor. The light emitted from the LED light sources travels in straight lines until it reaches the mirror, where it is reflected to the image plane. Due to specular reflection, the reflected light entering the camera has a strong intensity. As a result, bright spots appear in the image, as shown in Fig. 4(b). After applying binary masks to separate the bright regions, the centroids of the bright spots on the image were identified. The spatial positions of the bright points, which were recognised as the locations where specular reflection occurred, were calculated using the camera projection model. Then, the direction vectors of the reflected light, which originated from the bright points to the optical center, were determined. As the surface normal vectors of the mirror are all vertical facing downward, and the angle of incidence α_1 equals the angle of reflection α_2, the direction vectors of the incident light, which originated from the light-emitting points to the bright points, and the positions of the light-emitting points were confirmed. Consequently, the light direction vectors $\frac{\vec{L}}{|\vec{L}|}$ for each image point were estimated.

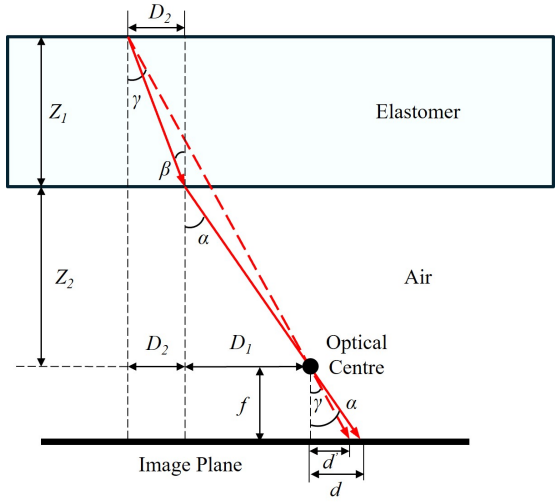

Fig. 5. Image correction for Light Refraction

B. Image Correction

Image distortion induced by light refraction is a common issue in VTS. Light refracts at the interfaces between the elastomer and the acrylic window, and between the elastomer and air due to their variable refractive indices. As a result, the camera captures distorted images. The distortion leads to inaccuracies in the measurement of contact geometry. Additionally, it complicates the subsequent calibration procedures, as traditional camera projection models are no longer applicable. Therefore, an image processing method to correct refraction-induced distortion is proposed. This method aims to restore the true geometric shapes while ensuring the corrected images conform to the camera projection model.

In GelPoLight, the acrylic window is relatively thin compared to the elastomer, and its refractive index is very close to that of the elastomer. Therefore, the acrylic window is not considered separately. The correction model is illustrated in Fig. 5. The red solid lines represent the actual light paths, and the red dashed lines represent the corrected light paths. The overall goal is to move pixels from their original positions d to the new positions d', making the images appear as if they were taken in the air.

The refractive index $n = 1.41$ of the elastomer is specified in the data sheet provided by the silicone rubber manufacturer. The height $Z_1 + Z_2$, the height Z_2, the focal length f and the position of the optical centre had been obtained in **Subsection A**. Therefore, the corrected positions were calculated as below:

$$\tan\alpha = \frac{d}{f}, \quad \sin\beta = \frac{\sin\alpha}{n}$$

$$\begin{aligned} d' &= f \cdot \tan\gamma \\ &= f \cdot \frac{D_1 + D_2}{Z_1 + Z_2} \\ &= f \cdot \frac{Z_2 \cdot \tan\alpha + Z_1 \cdot \tan\beta}{Z_1 + Z_2} \end{aligned} \tag{3}$$

In cases where multiple pixels were mapped to the same new position, an averaging method was applied. In Fig. 6, the membrane of the sensor was pressed by a steel ball bearing, and the contours of the indentation before and after correction were illustrated. The difference between the longest and shortest distances from the center to the contour was noticeably reduced, and the contour was corrected from an approximate ellipse to a circle. Additionally, the diameter of the indentation calculated from the corrected image using the camera projection model closely matched the true diameter of the ball.

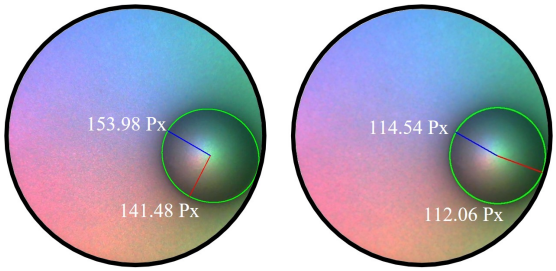

(a) Before Correction (b) After Correction

Fig. 6. Indentations Before and After Image Correction

C. Light Radiance

Although the LEDs chosen for GelPoLight have wide radiation angles, the light intensity across the membrane remains variable. Directly calculating spatial light intensities from LED radiation model is theoretically possible, but it involves many parameters which are hard to accurately obtain. Besides, the presence of unavoidable obstructions in the light path, such as dust, affected the precision of direct estimation. An experimental method involving a standard whiteboard was adopted to estimate the light intensity.

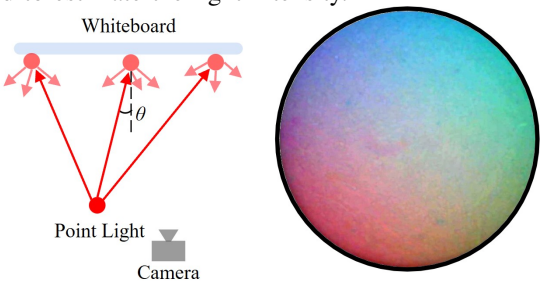

(a) Whiteboard under Point Lighting (b) Light Intensities Distribution

Fig. 7. Light Intensity Calibration by Whiteboard

As shown in Fig. 7(a), a diffuse reflection standard whiteboard was placed onto the top surface of the sensor under pressure. This procedure was conducted with the elastomer integrated in the sensor but before it was covered with the membrane. Since both contact surfaces of the whiteboard and the sensor are flat, the elastomer made full contact under pressure. Consequently, the lighting condition on the whiteboard was assumed to be the same as on the membrane. As the standard whiteboard closely approximates an ideal diffuse reflection surface, the reflection in this scenario was assumed to be Lambertian. The Eq. (1) can be rewritten as following:

$$I = \rho \cdot |\vec{L}| \cdot \cos \angle(\vec{L}, \vec{n}) \tag{4}$$

As the incident light direction vectors $\vec{L}$ have been obtained in **Subsection A**, and the surface normal vectors $\vec{n}$ of the whiteboard are all vertical, pointing downward, the angles between them $\theta = \angle(\vec{L}, \vec{n})$ were calculated. Since the whiteboard was assumed Lambertian surface, the reflectance factors ρ are constant. Therefore, the distribution of light intensity $|\vec{L}|$ across the membrane was determined:

$$|\vec{L}| = \frac{I}{\cos \theta} \tag{5}$$

The distribution of light intensities across the sensing surface of GelPoLight were visualised in Fig. 7 (b), where RGB values represent the corresponding colored light intensities.

D. Reflectance Function

For the non-ideal reflective membrane in GelPoLight, the relation between pixel values I and angles $\theta = \angle(\vec{L}, \vec{n})$ might not adhere to the cosine law, as described in Eq. (4). However, it should conform to a specific function, described as:

$$I = \rho \cdot |\vec{L}| \cdot \mathcal{G}(\angle(\vec{L}, \vec{n})) \tag{6}$$

The light intensity $|\vec{L}|$ has been obtained in **Subsection C**, and the reflectance factors ρ are assumed to be constant in this part. For later convenience, the angles θ were replaced by $\cos \theta$. Therefore, the Eq. (6) can be written as:

$$\cos \theta = \mathcal{R}(\frac{I}{|\vec{L}|}) \tag{7}$$

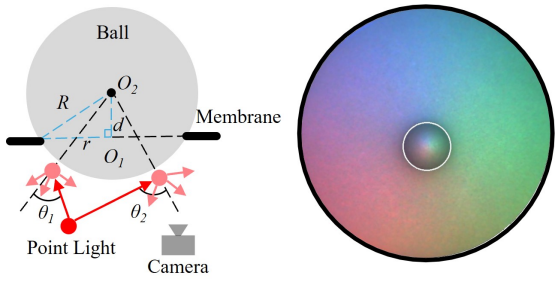

(a) Ball Pressing Model (b) Indentation Contour

Fig. 8. Reflectance Property Calibration by Ball Pressing

The following calibrations were performed to experimentally obtain the mapping $\mathcal{R}$. The experiments were conducted with the sensor fully assembled. As illustrated in Fig. 8(a), a bearing ball with a known radius R was pressed onto the sensing surface. A circular indentation appeared on the image due to the noticeable change in pixel values, as shown in Fig. 8(b). The center o_1 and radius r were obtained after identifying the contour of the circular indentation. Therefore, the distance d between the center of indentation o_1 and the center of the ball o_2 can be calculated as :

$$d = \sqrt{R^2 - r^2} \tag{8}$$

Consequently, the position of the ball center o_2 and the surface normal vectors on the indentation were determined. As the positions of the three light-emitting points were obtained in **Subsection A**, triplet $\cos\theta$ for each image point on the indentation were worked out. The experiment was repeated at several different locations on the membrane to enhance the dataset. The mapping between the processed pixel values $I_p = \frac{I}{|\vec{L}|}$ and $\cos\theta$ in three color channels were shown in fig. 9(a). After filtering out the outliers and averaging the results, the following look-up table was obtained, shown in fig. 9(b).

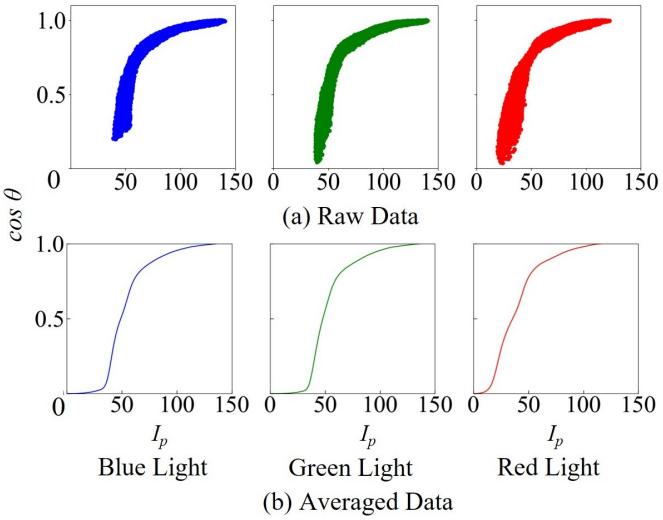

Fig. 9. Mapping Between Processed Pixel Values I_p and $\cos\theta$

E. Reflectance Factors

The reflectance factors ρ of the image points on the membrane were assumed to be constant in **Subsection D**. However, various factors such as fabrication inconsistencies and impurities in the aluminum powder can introduce errors. A method involving the comparison of theoretical pixel values and actual pixel values was applied to determine the reflectance factor for each image point on the membrane.

As shown in Fig. 10(a), the camera captured a background image of the membrane without contact. Since the membrane is flat, the surface normal vectors across the membrane are all vertical, pointing downward. As the light direction vectors have been obtained in **Subsection A**, the values of $\cos\theta$ for each background image point were determined. The light intensities $|\vec{L}|$ and the reflectance function $\mathcal{R}$ have been obtained in **Subsection C, D**.

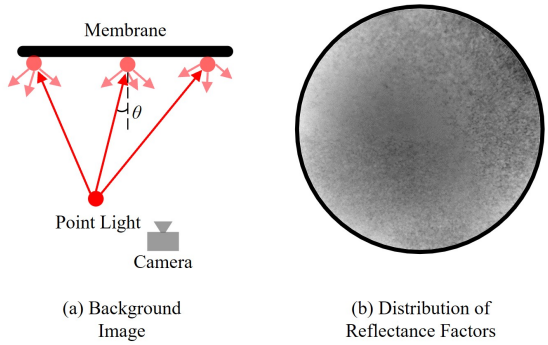

Fig. 10. Reflectance Factors Calibration

For each background image point, the pixel values can be obtained through theoretical approach and measured values. The theoretical pixel values I_t were obtained by substituting the values of $\cos\theta$ into Eq. (7), while the actual pixel values I were obtained directly from the background image. Since the reflectance factors were assumed to be constant in the theoretical approach, the actual reflectance factors ρ were calculated as below:

$$\rho = \frac{I}{I_t} \tag{9}$$

The distribution of reflectance factors ρ for GelPoLight was visualised in Fig. 10(b), where points with higher grayscale values represent higher reflectance factors. The method described above also compensates for the initial calibrations. The reflectance factors can be fed back into **Subsection D**, replacing the constant values ρ to improve the mapping. In practice, one iteration is sufficient to achieve satisfactory results.

F. Depth Map

For each image point, light direction vectors $\frac{\vec{L}}{|\vec{L}|}$, light intensities $|\vec{L}|$, reflectance functions $\mathcal{R}$, and reflectance factors ρ have been obtained in **Subsections A, C, D, and E**. Consequently, surface normal vectors can be calculated by substituting triplet pixel values I and solving the following equation:

$$\frac{\vec{L}}{|\vec{L}|} \cdot \vec{n} = \mathcal{R}\left(\frac{I}{\rho \cdot |\vec{L}|}\right) \tag{10}$$

We follow the approach of solving the Poisson equation to integrate the surface normal vectors $\vec{n}$ into the depth map. A fast Poisson solver with discrete sine transform was employed to accelerate the computations for real-time output [31]. The current version of GelPoLight is capable of achieving 10 Hz processing for images with a resolution of 1280×960.

VI. Experiments and Results

A. Tactile Sensing for Various Objects

GelPoLight was tested on various objects. As illustrated in Fig. 11, the sensor demonstrates high sensitivity to subtle deformations and effectively reconstructs depth maps for complex geometry.

B. Evaluation of 3D-reconstruction

The 3D-measurements of GelPoLight were evaluated using 3D printed models using a Form 3 + printer (Formlabs Inc., Somerville, Massachusetts, USA) with a resolution of 0.025 mm. We created cylindrical and rectangular cuboid models with flat bases, shown in Fig. 12 (a), expecting the sensor to display the 3D shapes of the indenters when they were fully pressed onto it. The dimensions of the models were used as the ground truth for evaluating reconstruction accuracy.

The experiments were conducted in both the planar and depth directions. In planar direction experiments, cylindrical and rectangular cuboid models with the same height but

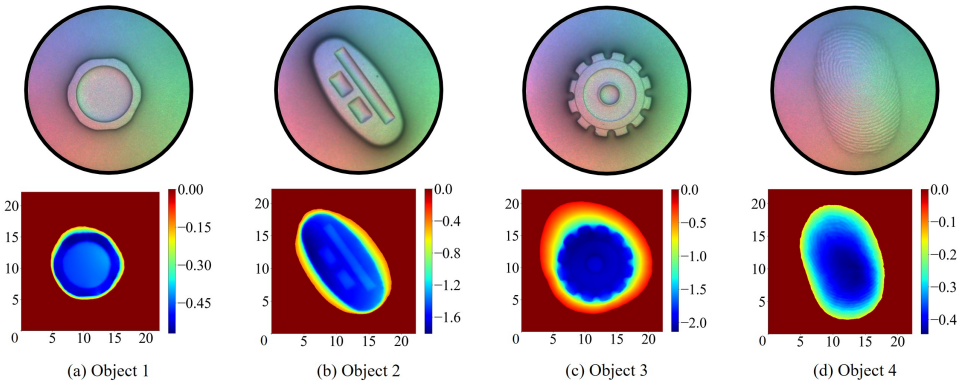

Fig. 11. Performance of Depth Map Reconstruction

varying diameters or side lengths of 3 mm, 4 mm, 5 mm, 6 mm, and 7 mm were tested 5 times in the same sensing region. Then, the same cylinder and cuboid models were tested in 25 random regions of the sensor. Similarly, in depth direction experiments, models with the same diameters or side lengths but with varying heights of 0.5 mm, 0.75 mm, 1 mm, 1.25 mm and 1.5 mm were tested 5 times in the same sensing region, and the same models were tested in 25 random regions of the sensor. Several illustrative examples for cylindrical cuboid pressed in depth direction are presented in Fig. 12 (b), which demonstrate that even as the indentation depth increases, the reconstruction effectively follows the original shape with minimal degradation caused by factors such as shadowing. The primary deviations observed are attributed to the viscoelastic nature of the silicone rubber, which causes deformation in the surrounding material under pressure.

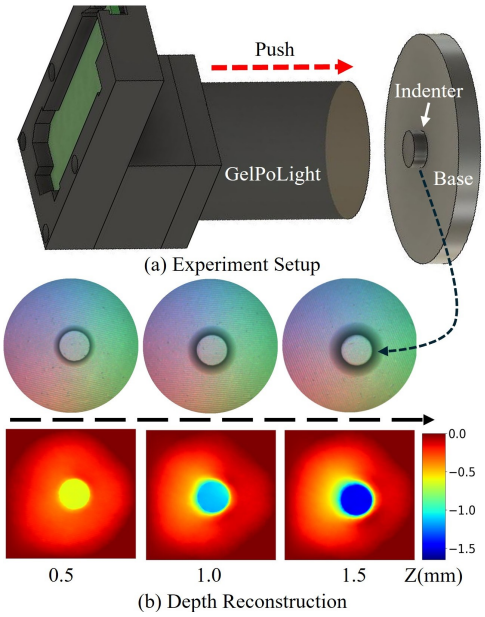

Fig. 12. Procedure for 3D Measurement Experiments

The results of the experiments are shown in Fig. 13. For both models and in random regions, the average errors between the measured dimensions of the sensor and those obtained from 3D printed models are approximately 5% in the planar direction and approximately 8% in depth direction. Additionally, the measurement exhibits better consistency in the planar direction, while there was greater fluctuation in depth direction.

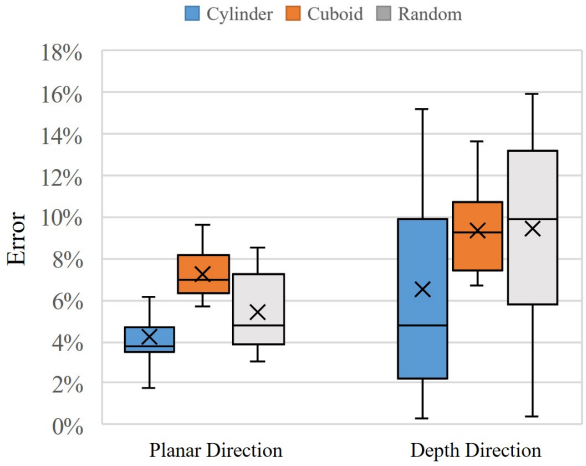

Fig. 13. Errors between the dimensions measured by GelPoLight and those obtained from the 3D-printed models in the experiments

VII. Discussions and Future Works

In this paper, we have demonstrated the advantages of point lighting for VBTS-PS. The calibration method has proven effective for 3D measurement of contact geometry. Further enhancements, such as implementing radiometric calibration of the camera, could potentially improve the estimation of light radiation distribution. Benefiting from point lighting, GelPoLight has much potential to be developed into various sizes and shapes. In future work, we will further refine our calibration method and explore applications of GelPoight in scenarios unattainable by previous VTS-PS.

The elastomer thickness and LED configuration should be carefully considered to prevent potential specular reflections of the light emitted by the LEDs at the air-elastomer interface from entering the camera, as it may distort the captured images of the reflective membrane.

The advantages of point lighting for VBTS-PS have been discussed primarily in the context of flat sensing surfaces. Point lighting also offers unparalleled benefits for sensors with curved sensing surfaces, as it can fully illuminate the entire surface, whereas directional lighting can only illuminate a portion of it. In future work, we will develop GelPoLight into curved sensing surfaces and accordingly adapt the working principle and calibration method.

REFERENCES

[1] P. Yu, W. Liu, C. Gu, X. Cheng, and X. Fu, "Flexible piezoelectric tactile sensor array for dynamic three-axis force measurement," *Sensors*, vol. 16, no. 6, p. 819, 2016.

[2] Y. Zhu, Y. Liu, Y. Sun, Y. Zhang, and G. Ding, "Recent advances in resistive sensor technology for tactile perception: A review," *IEEE Sensors Journal*, vol. 22, no. 16, pp. 15 635–15 649, 2022.

[3] T.-H.-L. Le, A. Maslyczyk, J.-P. Roberge, and V. Duchaine, "A highly sensitive multimodal capacitive tactile sensor," in *2017 IEEE International Conference on Robotics and Automation (ICRA)*, 2017, pp. 407–412.

[4] T. Li, J. Zou, F. Xing, M. Zhang, X. Cao, N. Wang, and Z. L. Wang, "From dual-mode triboelectric nanogenerator to smart tactile sensor: a multiplexing design," *ACS nano*, vol. 11, no. 4, pp. 3950–3956, 2017.

[5] N. Yao and S. Wang, "Recent progress of optical tactile sensors: A review," *Optics & Laser Technology*, vol. 176, p. 111040, 2024.

[6] W. Zhang, R. Singh, F.-Z. Liu, C. Marques, B. Zhang, and S. Kumar, "Waveflex biosensor: A flexible-shaped plasmonic optical fiber sensor for histamine detection," *IEEE Sensors Journal*, vol. 23, no. 19, pp. 22 533–22 542, 2023.

[7] I. S. Bayer, "Mems-based tactile sensors: materials, processes and applications in robotics," *Micromachines*, vol. 13, no. 12, p. 2051, 2022.

[8] M. K. Johnson and E. H. Adelson, "Retrographic sensing for the measurement of surface texture and shape," in *2009 IEEE Conference on Computer Vision and Pattern Recognition*. IEEE, 2009, pp. 1070–1077.

[9] R. J. Woodham, "Photometric method for determining surface orientation from multiple images," *Optical engineering*, vol. 19, no. 1, pp. 139–144, 1980.

[10] R. Li, R. Platt, W. Yuan, A. Ten Pas, N. Roscup, M. A. Srinivasan, and E. Adelson, "Localization and manipulation of small parts using gelsight tactile sensing," in *2014 IEEE/RSJ International Conference on Intelligent Robots and Systems*. IEEE, 2014, pp. 3988–3993.

[11] S. Dong, W. Yuan, and E. H. Adelson, "Improved gelsight tactile sensor for measuring geometry and slip," in *2017 IEEE/RSJ International Conference on Intelligent Robots and Systems (IROS)*. IEEE, 2017, pp. 137–144.

[12] S. Wang, Y. She, B. Romero, and E. Adelson, "Gelsight wedge: Measuring high-resolution 3d contact geometry with a compact robot finger," in *2021 IEEE International Conference on Robotics and Automation (ICRA)*, 2021, pp. 6468–6475.

[13] I. H. Taylor, S. Dong, and A. Rodriguez, "Gelslim 3.0: High-resolution measurement of shape, force and slip in a compact tactile-sensing finger," in *2022 International Conference on Robotics and Automation (ICRA)*. IEEE, 2022, pp. 10 781–10 787.

[14] W. Yuan, R. Li, M. A. Srinivasan, and E. H. Adelson, "Measurement of shear and slip with a gelsight tactile sensor," in *2015 IEEE International Conference on Robotics and Automation (ICRA)*, 2015, pp. 304–311.

[15] W. Li, M. Wang, J. Li, Y. Su, D. K. Jha, X. Qian, K. Althoefer, and H. Liu, "L^3 f-touch: A wireless gelsight with decoupled tactile and three-axis force sensing," *IEEE Robotics and Automation Letters*, vol. 8, no. 8, pp. 5148–5155, 2023.

[16] R. Li and E. H. Adelson, "Sensing and recognizing surface textures using a gelsight sensor," in *Proceedings of the IEEE Conference on Computer Vision and Pattern Recognition*, 2013, pp. 1241–1247.

[17] W. Yuan, M. A. Srinivasan, and E. H. Adelson, "Estimating object hardness with a gelsight touch sensor," in *2016 IEEE/RSJ International Conference on Intelligent Robots and Systems (IROS)*. IEEE, 2016, pp. 208–215.

[18] X. Jia, R. Li, M. A. Srinivasan, and E. H. Adelson, "Lump detection with a gelsight sensor," in *2013 World Haptics Conference (WHC)*. IEEE, 2013, pp. 175–179.

[19] M. Lambeta, P.-W. Chou, S. Tian, B. Yang, B. Maloon, V. R. Most, D. Stroud, R. Santos, A. Byagowi, G. Kammerer, D. Jayaraman, and R. Calandra, "Digit: A novel design for a low-cost compact high-resolution tactile sensor with application to in-hand manipulation," *IEEE Robotics and Automation Letters*, vol. 5, no. 3, pp. 3838–3845, 2020.

[20] E. Donlon, S. Dong, M. Liu, J. Li, E. Adelson, and A. Rodriguez, "Gelslim: A high-resolution, compact, robust, and calibrated tactile-sensing finger," in *2018 IEEE/RSJ International Conference on Intelligent Robots and Systems (IROS)*. IEEE, 2018, pp. 1927–1934.

[21] J. Zhao and E. H. Adelson, "Gelsight svelte: A human finger-shaped single-camera tactile robot finger with large sensing coverage and proprioceptive sensing," in *2023 IEEE/RSJ International Conference on Intelligent Robots and Systems (IROS)*. IEEE, 2023, pp. 8979–8984.

[22] B. Romero, F. Veiga, and E. Adelson, "Soft, round, high resolution tactile fingertip sensors for dexterous robotic manipulation," in *2020 IEEE International Conference on Robotics and Automation (ICRA)*, 2020, pp. 4796–4802.

[23] M. H. Tippur and E. H. Adelson, "Gelsight360: An omnidirectional camera-based tactile sensor for dexterous robotic manipulation," in *2023 IEEE International Conference on Soft Robotics (RoboSoft)*. IEEE, 2023, pp. 1–8.

[24] R. Patel, R. Ouyang, B. Romero, and E. Adelson, "Digger finger: Gelsight tactile sensor for object identification inside granular media," in *Experimental Robotics: The 17th International Symposium*. Springer, 2021, pp. 105–115.

[25] A. Padmanabha, F. Ebert, S. Tian, R. Calandra, C. Finn, and S. Levine, "Omnitact: A multi-directional high-resolution touch sensor," in *2020 IEEE International Conference on Robotics and Automation (ICRA)*, 2020, pp. 618–624.

[26] D. F. Gomes, Z. Lin, and S. Luo, "Geltip: A finger-shaped optical tactile sensor for robotic manipulation," in *2020 IEEE/RSJ International Conference on Intelligent Robots and Systems (IROS)*. IEEE, 2020, pp. 9903–9909.

[27] M. K. Johnson, F. Cole, A. Raj, and E. H. Adelson, "Microgeometry capture using an elastomeric sensor," *ACM Transactions on Graphics (TOG)*, vol. 30, no. 4, pp. 1–8, 2011.

[28] H. Jiang, Y. Yan, X. Zhu, and C. Zhang, "A 3-d surface reconstruction with shadow processing for optical tactile sensors," *Sensors*, vol. 18, no. 9, p. 2785, 2018.

[29] I. Andrussow, H. Sun, K. J. Kuchenbecker, and G. Martius, "Minsight: A fingertip-sized vision-based tactile sensor for robotic manipulation," *Advanced Intelligent Systems*, vol. 5, no. 8, p. 2300042, 2023.

[30] H. Kim, O. C. Kara, and F. Alambeigi, "A soft and inflatable vision-based tactile sensor for inspection of constrained and confined spaces," *IEEE Sensors Journal*, vol. 23, no. 23, pp. 29 605–29 618, 2023.

[31] R. Raskar, "Matlab code for poisson image reconstruction from image gradients," http://web.media.mit.edu/ raskar/photo/code.pdf, available online.

Chuang Lu received his B.S. degree in Thermal Power Engineering from Huazhong University of Science and Technology, China, in 2015, and the M.S. degree in Advanced Electronic and Electrical Engineering from Queen Mary University of London, UK, in 2022. He is currently pursuing a Ph.D. degree at University College London, U.K.. His research interests include tactile sensing and medical robotics.

Ziting Liang (Graduate Student Member, IEEE) received the B.S. degree in mechatronic engineering from Qinghai University, China, in 2018 and the M.S. degree in mechanical engineering from Xi'an Jiaotong University, China, in 2021. He is currently pursuing a Ph.D. degree at University College London, U.K.. His research interests include medical robotics and MR compatible robotics.

Danail Stoyanov (Fellow, IEEE) received the Ph.D. degree in computer science from the Imperial College London, London, U.K., in 2006, where he specialised in medical image computing. He is currently a Professor of Robot Vision with the Department of Computer Science, University College London, London, U.K., the Director of UCL WEISS, Royal Academy of Engineering Chair in Emerging Technologies and Head Scientist at Digital Surgery, Medtronic.

Agostino Stilli (Member, IEEE) received his Ph.D. degree in Robotics from King's College London, U.K, in 2017. He is currently an Associate Professor in Medical and Soft Robotics in the Department of Medical Physics and Biomedical Engineering at University College London, U.K., with UCL WEISS and the UCL Robotics Institute. He is Co-Investigator for Robotics in the Surgical Robot Vision research group and a Rosetrees/Stoneygate Enterprise Fellow.